J Mater Sci: Mater Electron (2012) 23:1001–1010
DOI 10.1007/s10854-011-0537-0

Vickers hardness measurements and some physical properties of Pr_2O_3 doped Bi-2212 superconductors

E. Asikuzun · O. Ozturk · H. A. Cetinkara · G. Yildirim · A. Varilci · M. Yılmazlar · C. Terzioglu

Received: 8 August 2011 / Accepted: 1 October 2011 / Published online: 11 October 2011

Abstract This study deals with the effect of Pr_2O_3 addition on the structural, superconducting and mechanical properties of Bi-2212 superconductor by means of X-ray diffraction analysis (XRD), scanning electron microscopy (SEM), electron dispersive X-ray (EDX), Vickers microhardness and resistivity measurements. The samples studied are prepared using the standard solid-state reaction method. Onset transition temperatures (T_c^{onset}) of the samples are estimated from the dc resistivity measurements. Furthermore, the phase ratio and lattice parameters a and c are determined from XRD patterns when the microstructure, surface morphology and element composition analyses of the samples are investigated by SEM and EDX measurements, respectively. Additionally, vickers microhardness, elastic modulus, yield strength and fracture toughness values of the samples are deduced from microhardness measurements. It is found that T_c^{onset} values of the samples increase from 87 to 97 K with the Pr_2O_3 addition. According to the refinement of cell parameters done by considering the structural modulation, the doping is confirmed by both an increase of the lattice parameter a and a decrease of the cell parameter c of the samples in comparison with that of the pure sample. As for SEM measurements, it is obtained that the surface morphology and grain connectivity degrade with the increase of the Pr_2O_3 addition. Moreover, EDX images show that the elements used for the preparation of samples distribute homogeneously and the Pr atoms enter into the crystal structure by replacing Sr atoms. To sum up, the Pr_2O_3 addition is found to suppress the mechanical, microstructural and superconducting properties of the Bi-2212 superconductor.

E. Asikuzun · O. Ozturk (✉)
Department of Physics, Faculty of Arts and Science, Kastamonu University, 37100 Kastamonu, Turkey
e-mail: oozturk@kastamonu.edu.tr

H. A. Cetinkara
Department of Physics, Faculty of Arts and Science, Mustafa Kemal University, 31100 Hatay, Turkey

G. Yildirim · A. Varilci · C. Terzioglu
Department of Physics, Faculty of Arts and Science, Abant Izzet Baysal University, 14280 Bolu, Turkey

M. Yılmazlar
Faculty of Education, Sakarya University, 54300 Hendek, Sakarya, Turkey

1 Introduction

Since the discovery of superconductivity, researchers have tried to improve the superconducting, mechanical and structural properties of the superconductor materials to make them suitable for high temperature and magnetic field applications [1–4]. In particular, Bi–Sr–Ca–Cu–O (BSCCO) superconductor materials discovered by Maeda et al. [5] have widely been investigated owing to the fact that the interest in both the fundamental research and applications in technology and industry of these materials in the last decades stems from their remarkable smaller power losses, high current and magnetic field carrying capacity, optical and electronic properties [6–14]. The BSCCO system obtaining a layered structure has three different phases with respect to its chemical compositions, the Bi-2201 phase ($n = 1$, $Tc \approx 20$ K), the Bi-2212 phase ($n = 2$, $Tc \approx 85$ K) and the (Bi, Pb)-2223 phase ($n = 3$, $Tc \approx 110$ K) [15]. Among the Bi-based superconductors, the double layered cuprate (Bi-2212) is superior to the others because of the better thermodynamic stability, lesser

weak link problems [16] and relatively invariant of the oxygen stoichiometry with respective to cationic doping [17]. Further, although the Bi-2212 materials play an important role on the preparation of long wires and tapes, the applications of them in magnetic field and high temperatures are reported to limit because of their structural layer, very low charge carrier density, strong anisotropic properties, extremely short coherence length (ξ) and large penetration depth (λ) [16, 18]. Similarly, the Bi-2212 superconductors have relatively poor mechanical properties, limiting the use of these materials in most of practical applications [19]. Hence, several methods have been studied to improve these properties of the materials for years. The rare-earth (RE) doping in the superconductor materials is one of the most preferred methods. The doping may lead to increase the number of charge carriers (either holes or electrons) in the material and so the superconducting properties might be enhanced. Moreover, mechanical properties such as the hardness, elastic modulus, yield strength, fracture toughness, brittleness index and ductility are also important parameters for industrial applications of the superconductor materials [20]. Indentation microhardness measurements are convenient method to investigate the mechanical properties.

The aim of this study is to investigate the role of Pr addition on the structural, superconducting and mechanical properties of Bi-2212 ceramics by means of the dc electrical resistivity measurements for electrical and superconducting properties, microhardness measurements for mechanical properties, XRD measurements for the phase composition and lattice parameters and scanning electron microscopy (SEM) for microstructure examination of the samples produced in this work.

2 Experimental analysis

The starting materials in this work are commercially available powders of Bi-2212 and Pr_2O_3 (Alfa Aesar Co., Ltd. 99.9% purity). The Pr-added Bi-2212 samples are prepared at 0.1, 0.3, 0.5, 0.7 and 1.0% doping concentration by the conventional solid–state reaction method. The Pr_2O_3 and stock powder are weighed in stoichiometric proportion and mixed in an agate mortar for 4 h to obtain homogeneous mixture. After mixing process, the homogeneous mixture of powders is pressed under 10 tons to make the sample 13 mm in diameter. The annealing process is carried out at 840 °C for 50 h in programmable tube furnace. The heating and cooling rates of the furnace are adjusted to be 5 and 3 °C/min, respectively. Hereafter, we will use the abbreviations Pure, Pr0.1, Pr0.3, Pr0.5, Pr0.7 and Pr1.0, respectively. All the calcinations and sintering processes of the samples are performed by using a programmable tube furnace (Protherm). For comparison, an undoped sample (Pure) is also subjected to the same annealing conditions.

In this study, the dc resistivity measurements are performed on the sample with the four-probe method. Both voltage and current contacts were made with silver paint in order to minimize the contact resistance. We measure the temperature (50–120 K) dependence of resistivity of the samples by running 5 mA DC current through the sample in the cryostat. A temperature value, where the resistivity starts to decrease sharply, is determined to be the critical temperature (T_c^{onset}) of the samples. Moreover, the phase composition of the samples is characterized by XRD method using a Rigaku D/Max-IIIC XRD with Cu Kα radiation ($\lambda = 1.5418$ Å) in the range $2\theta = 3$–$60°$ at a scan speed of 3°/min and a step increment of 0.02° at room temperature. Phase purity and lattice parameters are deduced from the XRD patterns. The accuracy in determining the lattice parameters (a and c) was determined to be ± 0.0001 Å. In addition, the grain connectivity and surface morphology of the samples are examined by means of a Jeol scanning electron microscope (SEM) JEOL 6390-LV, operated at 20 kV, with a resolution power of 3 nm. The elemental compositions (in the percent) and distributions (homogeneously or not) of the samples studied are also investigated by an Oxford X-ray micro-probe analysis connected to SEM (EDX).

Microhardness measurements of the samples produced are performed in air by using a digital microhardness tester (SHIMADZU) at room temperature. The applied load is varied within the range 0.245–2.940 N for a peak-load time of 10 s and the diagonals of indentation are measured with an accuracy of ± 0.1 μm. The values of Vickers microhardness are determined with an average of 20 readings at different locations of specimen surfaces. Moreover, the average particle sizes of the samples produced in this work are found to be in the range from a few micrometers up to 8 μm. Minimum average particle size of 4.6 μm is obtained for pure sample as against 8 μm, respectively, for the sample doped with 0.1 wt% Pr.

3 Results and discussions

3.1 XRD analysis

The XRD patterns of the samples prepared in this work are given in Fig. 1. The corresponding (h k L) Miller indices belonging to Bi(Pb)-2212 main lines are shown in the diagrams. As seen from the figure, all the samples exhibit the polycrystalline superconducting phase with more intensity of diffraction lines with increasing the Pr addition. Furthermore, no secondary phase containing Pr or any

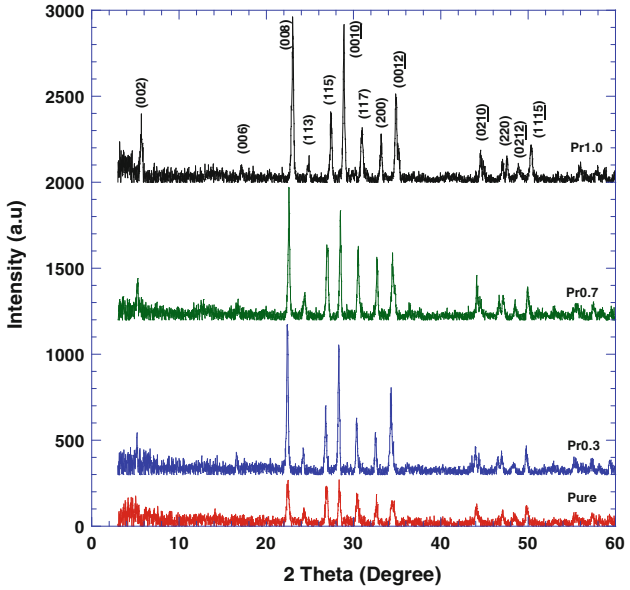

Fig. 1 XRD patterns of the Pure, Pr0.3, Pr0.7 and Pr1.0 samples

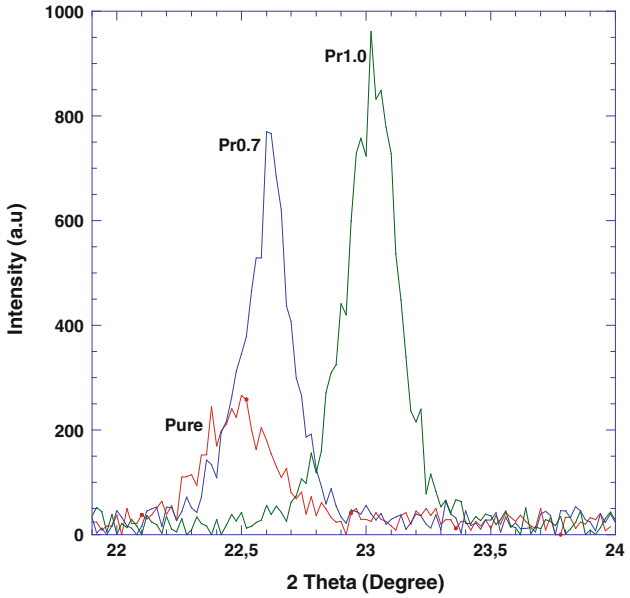

Fig. 2 XRD peaks for the (008) plane

other cation is observed even up to $x = 1$, showing that the Pr atoms are successfully introduced to the microstructure of the Bi-2212 phase [21–23]. The peak intensity of the samples doped increases regularly and other peaks such as (002) and (006) start to appear completely as the Pr addition increases. In particular, (008) peak shifting to greater angle reaches its top point (Fig. 2), revealing that why the superconducting properties suppress with the Pr doping in the system. Moreover, the lattice parameters a and c are calculated using the least square method through d values and (h k L) planes for tetragonal unit cell structure. The variation of lattice constants a and c with Pr concentration in the Bi-2212 samples is depicted in Fig. 3a, b. It is apparent from the figure that a systematic expansion in the a-axis length is observed while a regular contraction in the c-axis length is obtained with the increase in the Pr addition. It is well known that the increment of charge carriers (electrons) in high-temperature superconductors leads to the increase of the oxygen content in the system. The excess oxygen is captured by Bi–O planes of the sample due to the oxygen deficiency in these planes and the positive charges in the planes start to decrease. Therefore, the bond between the planes becomes stronger and stronger. As a result, the size of Bi–O planes and the length of c-axis decrease [22, 24–26], confirming that the Bi-2212 superconductors are suitable for the applications at higher temperature and higher fields [27]. On the other hand, the lattice parameter a is controlled by the length of in-plane Cu–O bond [28]. The length may be expanded or contracted with the change of the electrons into antibonding orbital. In our system this bond length is expanded because of the partial replacement of Cu^{2+} ions by Pr^{3+} ions, leading to an increase in the lattice parameter a, and a decrease in the lattice constant c. According to the results, the Bi-2212 phase decreases while the Bi-2201 phase starts to enhance with the increase of the Pr addition; however, Fig. 1 assures that the Bi-2212 phase is dominant for all the samples produced.

3.2 Hole-carrier concentration calculation

Charge carriers, both holes (p) and electrons (n), are in charge of the conductivity of the materials. The hole-carrier concentrations per Cu ion, p, are calculated by using the following relation,

$$P = 0.16 - \left[\left(1 - \frac{T_c}{T_c^{\max}}\right) \Big/ 82.6\right]^{1/2} \quad (1)$$

where $T_c^{\max}$ is taken as 85 K for Bi-2212 phase [29] and T_c values are deduced form Fig. 4. The carrier concentrations calculated are also tabulated in Table 1. As seen from the table, the hole-carrier concentrations are found to decrease with the increasing Pr addition. In other words, the critical temperature of the pure sample obtaining the greatest hole-carrier concentration is observed to be higher than the others (Table 1).

3.3 SEM and EDX analyses

The surface structure, orientations of the grains and accumulation in the grain boundaries of the Pure and Pr1.0 samples were investigated by SEM pictures taken in the secondary electron image mode. The micrographs in Fig. 5 illustrate that the surface morphology changes with

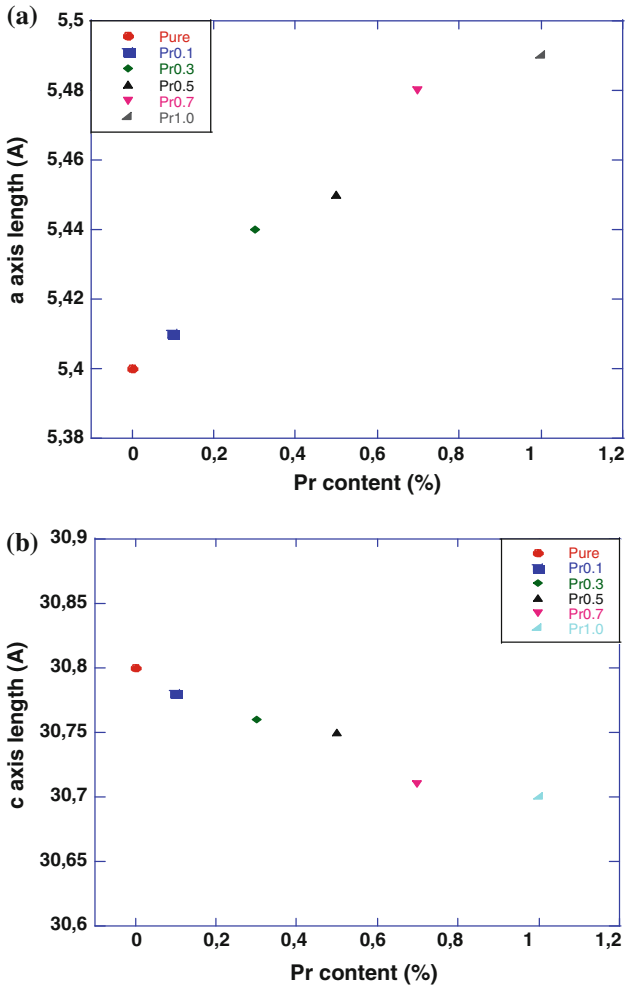

Fig. 3 Variation of lattice parameters as a function of Pr content

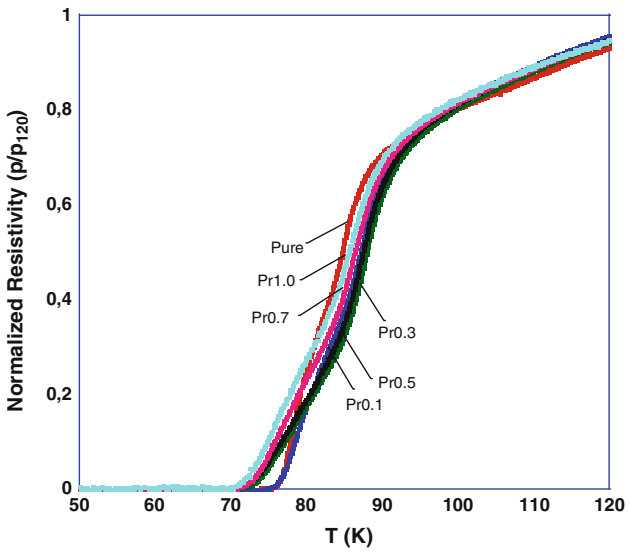

Fig. 4 Normalized resistivity as a function of temperature curves for the samples

addition of the Pr atoms in the Bi-2212 system. As seen from the figure, the granular morphology of all the samples produced indicates the clear and flaky grains with layered growth (basic characteristic of Bi-2212 phase formation in SEM photographs). However, the texturing and layered grain growth of the pure sample are found to be better compared to the doped samples. On the other hand, the most porous structure and softest surface are observed in the Pr1.0 sample because the platelet grains linked well in the sample is degraded with the increasement of the Pr addition due to the random orientation and weak links between the grains [30].

The elemental composition analyses of the samples were analytically investigated by the electron dispersive X-ray (EDX). Figure 6 gives Bi, Sr, Ca, Cu, O, and Pr element composition mappings taken on the surface of Pure and Pr1.0 samples studied in this work. As can be seen from the figures, no differences appear between the samples except for Pr peak, indicating that the Pr is incorporated into the crystalline structure of the samples. Moreover, the elements used for the preparation of samples are observed to distribute homogeneously (Fig. 6a, b). Nevertheless, it is apparent from the same figures that Sr concentration in Pr1.0 sample compared to other element compositions is found to decrease rapidly. Based on the results of EDX, the Pr atoms enter into the crystal structure by replacing Sr atoms [31].

3.4 Electrical resistivity measurements

The temperature dependence of normalized resistivity ($\rho - T$) of pure and Pr-doped samples ($0 \leq x \leq 1$) produced in this work is given in Fig. 4. It is observed that all the samples show metallic behavior above the T_c^{onset} temperature ($T \geq 100$ K). The room temperature (at 300 K) resistivity of the samples is listed in Table 1. As seen from the table, the resistivity systematically increases to a maximum (27.2 mΩ cm) as against 4.2 mΩ cm for the pure sample with the increase in Pr-content because of the shrink of the grains. Furthermore, the T_c^{onset} values (starting-point criterion) estimated from the $\rho - T$ plots are plotted against Pr content (see Fig. 7). It is visible that the T_c^{onset} value enhances considerably with the increase in the Pr content and reaches a maximum for the Pr1.0 sample. The T_c^{onset} is found to be about 87 K for the pure sample whereas the maximum T_c^{onset} of 97 K is obtained for the Pr1.0 sample.

3.5 Vickers microhardness measurements

We measure the diagonal length as a function of test load to understand the role of Pr addition on the mechanical properties of the samples produced in this work. As it is

Table 1 XRD and resistivity measurement results for the samples

Samples	a (Å)	c (Å)	Volume fraction (%)		T_c^{onset} (K)	Resistivity at 300 K (Ω.mm)	Hole concentration p
			2212–2201				
Pure	5.40	30.80	90.0	10.0	87	0.0047	0.125
Pr0.1	5.41	30.78	89.0	11.0	94	0.0060	0.122
Pr0.3	5.44	30.76	87.6	12.4	95	0.0074	0.116
Pr0.5	5.45	30.75	86.2	13.8	95.5	0.0075	0.115
Pr0.7	5.48	30.71	82.1	17.9	96	0.0076	0.115
Pr1.0	5.49	30.70	80.8	19.2	97	0.0079	0.113

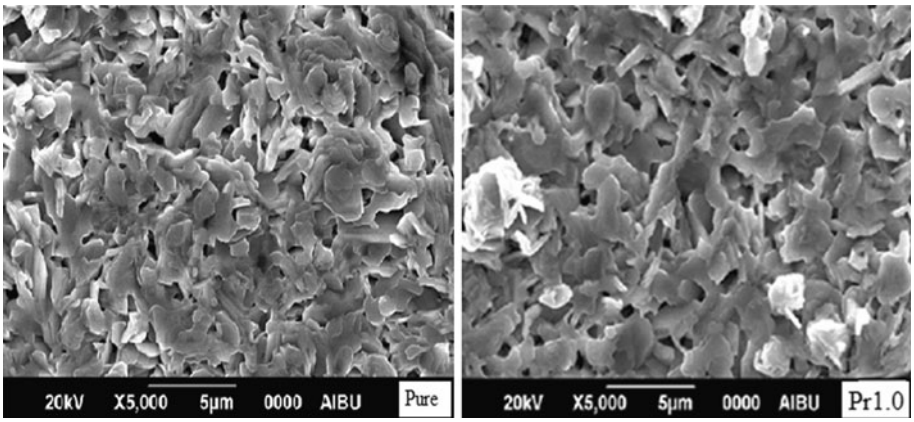

Fig. 5 SEM micrograph of Pure and Pr1.0 samples

well known, conventional Vickers microhardness measurements are composed of applying a load F on the test material by means of a geometrically defined indenter and after the indenter is removed, measuring the characteristic dimension, d, of the resultant impression.

The Vickers microhardness values of different applied loads in the range of 0.245–2.940 N are calculated using the following equation,

$$H_v = 1854.4\left(\frac{F}{d^2}\right) \quad \text{(GPa)} \tag{2}$$

where H_v is the Vickers hardness in GPa, F is the applied load in Newton, and d (in μm unit) is the diagonal length of the indentation. The Vickers hardness (H_v), elastic modulus (E), yield strength (Y) and fracture toughness (K_{IC}) computed by means of Eqs. 2–5 are listed in Table 2.

$$E = 81.9635H_V \tag{3}$$

$$Y \approx H_V/3 \tag{4}$$

$$K_{IC} = \sqrt{2E\gamma} \quad (\gamma, \text{ surface energy}) \tag{5}$$

Figure 8 illustrates the variation of microhardness as a function of the applied load for all the samples produced. It is apparent from the figure that the microhardness values are dependence of the Indentation load (ISE, Indentation Size Effect) and Pr addition. In other words; there is a decrease in the values of microhardness with the increase in the applied load and Pr content, confirming the weak grain boundaries, impurity phases and irregular grain orientation distribution [32].

The load dependence can be explained by two different methods: the elastic portion and energy dissipative processes. In the first method, the indentation contains an elastic portion. The elastic part of the deformation is relaxed upon unloading, accounted for by adding an elastic component, d_e, to the measured plastic indentation semidiagonal, d_p. Therefore the true hardness value, H_0, can be found using the following formula [33]:

$$H_0 = 1854.4\left[\frac{F}{(d_p + d_e)^2}\right] \quad \text{(GPa)} \tag{6}$$

As seen from the equation, the measured indentation diagonals should be linear with the square root of the applied load and the slope of such a curve is proportional to $(H_0)^{1/2}$ and the elastic part of the indentation semidiagonal (d_e) can be estimated from the vertical intercept of the curve obtained. Moreover, the applied load dependence of the indentation diagonals for all the samples is reinvestigated with the aid of $F^{1/2}$ versus d_p plots (Fig. 9). Furthermore,H_0, d_e and the estimated linear regression coefficients (LRC) values calculated for the samples are given in Table 3 in detail.

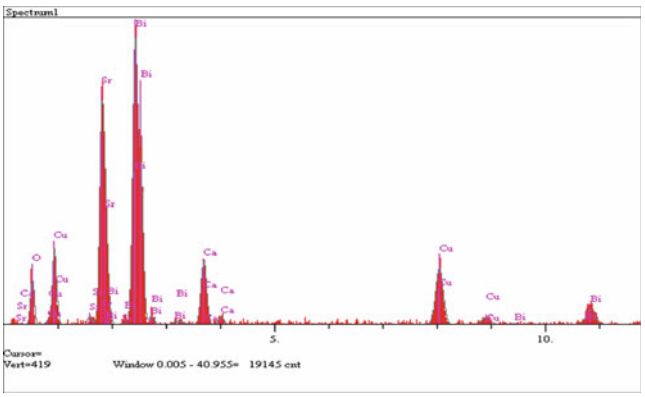

Elt.	Intensity (c/s)	Conc.
O	15.1	13.5
Ca	29.2	3.9
Cu	37.7	11.9
Sr	78.8	26.0
Bi	12.9	44.7
		100.0

(a) Pure

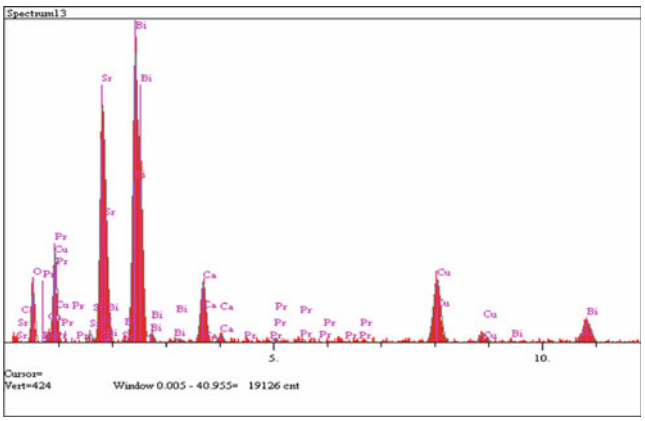

Elt.	Intensity (c/s)	Conc.
O	14.1	13.4
Ca	24.6	3.5
Cu	34.7	11.6
Sr	70.2	24.9
Pr	1.9	1.4
Bi	12.5	45.4
		100.0

(b) Pr1.0

Fig. 6 EDX patterns of **a** Pure and **b** Pr1.0 samples

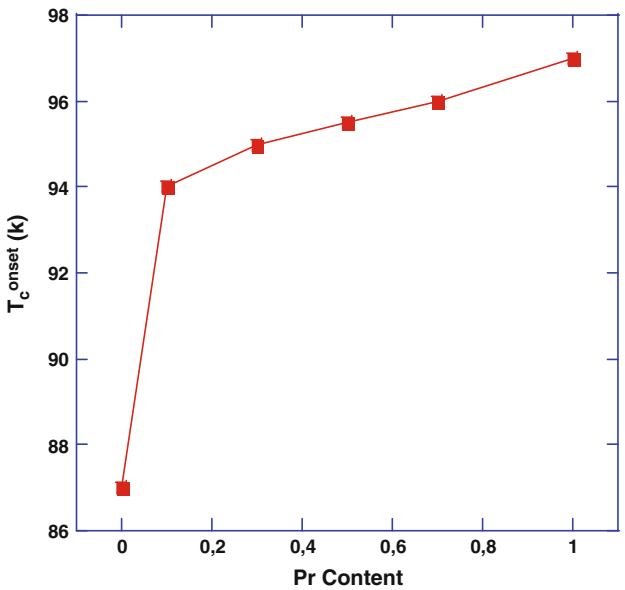

Fig. 7 Variation of T_c of the samples with Pr-content

In this study, true microhardness of the undoped sample (0.977 GPa) is obtained to be lower than the hardness results (1.018–1.038 GPa) in the plateau region (saturated region). This behaviour is observed in other samples produced. According to the results, the true value of hardness is lower than that of the traditionally calculated ones. Although the experimental data are truly fitted with the theoretical data (Fig. 9), this model is not suitable for our results because of the difference between the calculated results and true hardness values [34].

On the other hand, the second method considering energy dissipative processes during the indentation rather than elastic processes is applied consistently to the measured data [34, 35]. In this method, a true microhardness defined by subtracting a dissipative part, F_0, from the applied load can be calculated as follow:

$$H_v = 1854.4\left(\frac{F - F_0}{d^2}\right) \quad \text{(GPa)} \tag{7}$$

Figure 10 gives the variation of the applied load as a function of the square of the impression semidiagonal length for the samples studied in this work. It is visible from the figure that a good linear relationship is noticed for all the samples. While the slope of each line coincides with the load independent hardness constant (H_0), the vertical intercept of each line shows the sample resistance pressure (F_0). The true hardness, F_0, H_0 and LRC values are

Table 2 The calculated load dependent H_v, E, Y and K_{IC} for the samples

Samples	Load (N)	d (μm)	H_v (GPa)	E (GPa)	Y (GPa)	K_{ic} (Pa/m$^{1/2}$)
Pure	0.245	18.90	1.271	104.17	0.423	684.66
	0.490	28.16	1.145	93.84	0.381	649.98
	0.980	40.65	1.099	90.07	0.366	636.64
	1.960	59.16	1.038	85.07	0.346	618.72
	2.940	71.91	1.018	83.43	0.339	612.72
Pr0.1	0.245	19.77	1.162	95.24	0.387	897.62
	0.490	28.58	1.112	91.14	0.370	878.09
	0.980	43.75	0.950	77.86	0.316	811.60
	1.960	64.30	0.879	72.04	0.293	780.67
	2.940	80.56	0.841	68.93	0.280	763.64
Pr0.3	0.245	20.61	1.069	87.61	0.356	847.58
	0.490	30.15	0.999	81.88	0.333	819.39
	0.980	45.68	0.870	71.30	0.290	764.63
	1.960	67.97	0.786	64.42	0.262	726.80
	2.940	87.35	0.715	58.60	0.238	693.19
Pr0.5	0.245	21.45	0.987	80.89	0.329	888.53
	0.490	31.45	0.918	72.04	0.293	838.51
	0.980	47.34	0.810	66.39	0.270	804.96
	1.960	69.15	0.760	62.29	0.253	779.71
	2.940	89.41	0.682	55.89	0.227	738.57
Pr0.7	0.245	22.99	0.859	70.40	0.286	782.61
	0.490	34.38	0.768	62.94	0.256	739.98
	0.980	52.25	0.665	54.50	0.221	688.58
	1.960	76.97	0.613	50.24	0.204	661.12
	2.940	97.56	0.573	46.96	0.191	639.18
Pr1.0	0.245	23.55	0.819	67.12	0.273	821.72
	0.490	34.54	0.761	62.37	0.253	792.11
	0.980	54.95	0.601	49.26	0.200	703.95
	1.960	79.08	0.581	47.62	0.193	692.13
	2.940	100.72	0.537	44.01	0.179	665.38

deduced by Eq. 7 and are tabulated in Table 4. As seen from the table, the H_0 values of the samples are found to decrease while the F_0 values are obtained to increase with the increase in the Pr doping. Moreover, the greatest LRC value is obtained to be 0.99987 for Pr0.1 sample whereas the smallest one is observed to be 0.99935 for the Pr1.0 sample. According to the experimental observations, the diagonal length is found to be strictly dependent on the applied load, also. This expression can be identified with the following relation [36]:

$$\frac{F}{d} = H_0 d + \gamma \tag{8}$$

Figure 11 illustrates the values of F/d versus diagonal length of indentation, d for all the samples. One can observe from the figure that there is an excellent linear relationship for the small applied loads. The slop of the lines corresponds to the true hardness (H_0) while the intercept of the lines indicates the surface energy (γ) value. The obtained values for H_0, γ and LRC are depicted in Table 5. It is apparent from the table that whereas the true hardness values decrease, the surface energies enhance dramatically with the increase of the Pr addition, indicating the dissipation energy of the cracks at the interfaces [37, 38].

Additionally, the load independent values of elastic modulus (E_0), yield strength (Y_0) and fracture toughness (K_{IC}) of the samples are calculated by means of the true microhardness (load independent, H_0) and listed in Table 6. As seen from the table, the load independent values of E_0 and Y_0 are observed to decrease with the increase in the Pr content [39]. Similar observations in the elastic modulus, yield strength and fracture toughness are also reported in the literature [40]. Further, the fracture toughness is obtained to increase as the Pr addition increases. According to the results, the load independent values calculated are found to be lower than the load dependent values (Table 2).

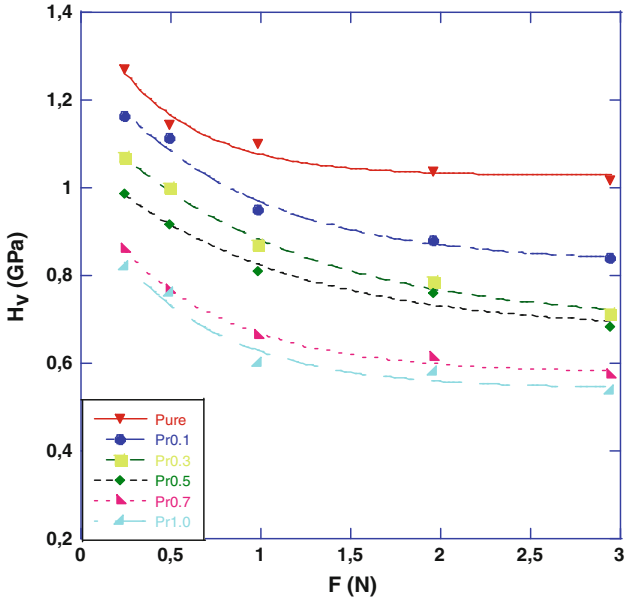

Fig. 8 The variations of microhardness with load for the samples

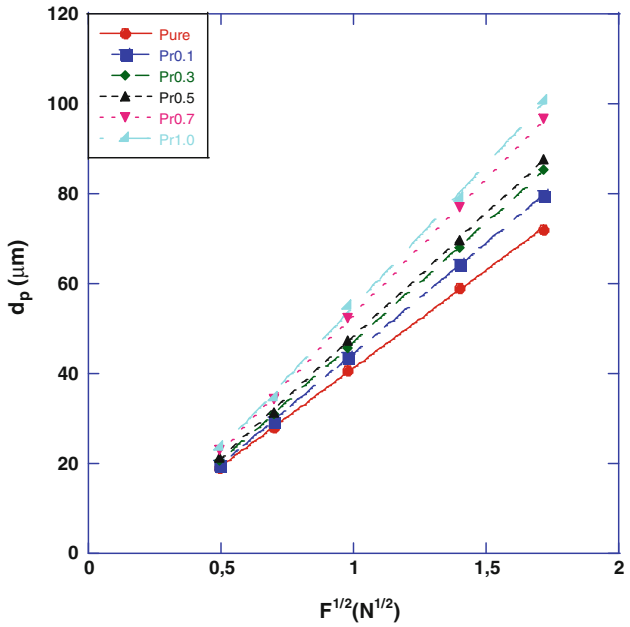

Fig. 9 Plots of diagonal length versus square root of applied loads for the samples

Table 3 Best-fit results of experimental data according to Eq. 6

Samples	H_0 (GPa)	d_e (μm)	LRC	H_v (GPa)
Pure	0.977	2.33	0.99983	1.018–1.038
Pr0.1	0.765	4.68	0.99996	0.841–0.879
Pr0.3	0.660	5.89	0.99992	0.715–0.786
Pr0.5	0.625	6.06	0.99978	0.682–0.760
Pr0.7	0.508	7.27	0.99988	0.573–0.613
Pr1.0	0.463	8.37	0.99929	0.537–0.581

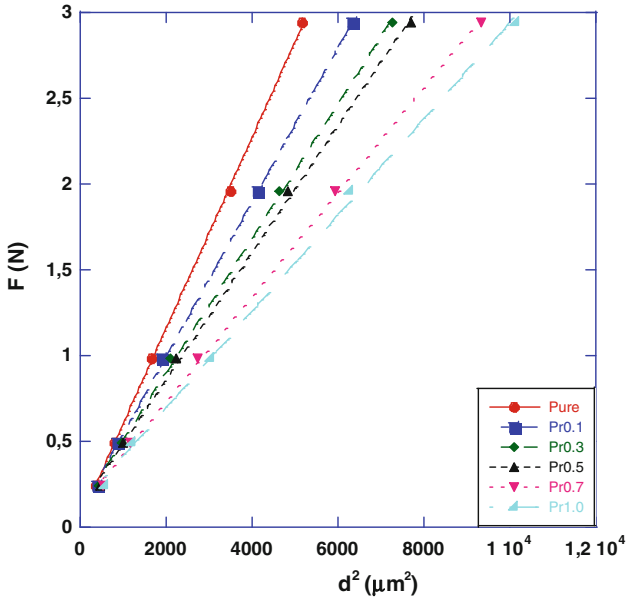

Fig. 10 Graph of the applied load against the square of the diagonal length for the samples

Table 4 Best-fit results of experimental data according to Eq. 7

Samples	H_0 (GPa)	F_0 (N)	LRC	H_v (GPa)
Pure	1.031	0.046	0.99983	1.018–1.038
Pr0.1	0.834	0.093	0.99987	0.841–0.879
Pr0.3	0.723	0.117	0.99945	0.715–0.786
Pr0.5	0.686	0.119	0.99938	0.682–0.760
Pr0.7	0.565	0.121	0.99963	0.573–0.613
Pr1.0	0.519	0.134	0.99935	0.537–0.581

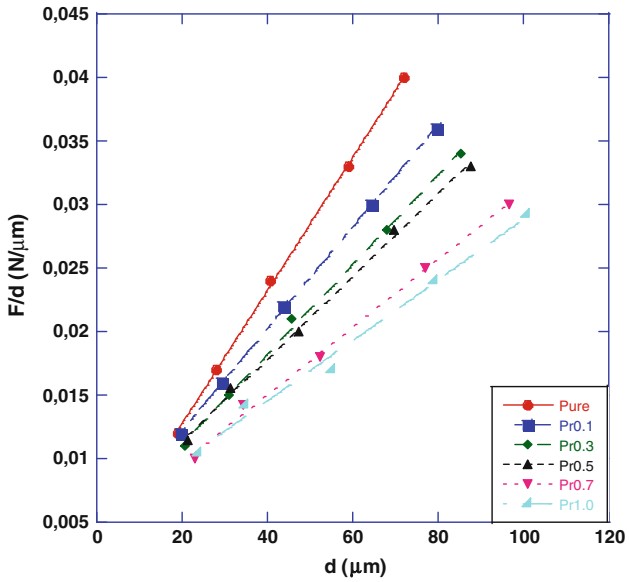

Fig. 11 Plots of *F*/*d* versus d for the samples

Table 5 Best-fit results of experimental data according to Eq. 8

Samples	H_0 (GPa)	$\gamma \times 10^{-3}$ (N/μm)	LRC	H_v (GPa)
Pure	0.971	2.25	0.99972	1.018–1.038
Pr0.1	0.741	4.23	0.99987	0.841–0.879
Pr0.3	0.652	4.10	0.99884	0.715–0.786
Pr0.5	0.600	4.88	0.99855	0.682–0.760
Pr0.7	0.493	4.35	0.99832	0.573–0.613
Pr1.0	0.441	5.00	0.99517	0.537–0.581

Table 6 The calculated load independent H_0, E_0, Y_0 and K_{IC} for the samples

Samples	H_0 (GPa)	E_0 (GPa)	Y_0 (GPa)	K_{ic} (Pa/m$^{1/2}$)	H_v (GPa)
Pure	0.971	79.586	0.323	598.4	1.018–1.038
Pr0.1	0.741	60.734	0.247	716.8	0.841–0.879
Pr0.3	0.652	53.440	0.217	661.9	0.715–0.786
Pr0.5	0.600	49.178	0.200	692.8	0.682–0.760
Pr0.7	0.493	40.408	0.164	592.9	0.573–0.613
Pr1.0	0.439	35.981	0.146	601.6	0.537–0.581

Moreover, this study reports that the Vickers hardness of the samples prepared in this work exhibits the typical indentation size effect (ISE) behavior [41–46]. The microhardness value calculated decreases non-linearly as the applied load decreases until 2 N, and then it tends to attain saturation. According to Khalil [47], this phenomenon is expressed in two parts; (a) at larger indention loads, the Vickers hardness registers smaller values, this observation may result from the presence of weak grain boundaries of the superconducting ceramics; (b) at smaller indention loads, the Vickers hardness records higher values, this is attributed to the fact that the measured hardness value is more indicative of the monocrystalline state without interference from grain boundaries.

4 Conclusion

In this study, it is investigated that how the Pr_2O_3 addition affects the structural, superconducting and mechanical properties of Bi-2212 superconductor via the X-ray diffraction analysis, scanning electron microscopy, electron dispersive X-ray, Vickers microhardness and resistivity measurements. The results show that the Pr_2O_3 addition degrades the mechanical, microstructural and superconducting properties of the Bi-2212 superconductor and the following statements are concluded:

- The Pr addition enhances the onset transition temperature (T_c^{onset}).
- SEM images point out that the best surface morphology, largest grain size and grain connectivity are observed for the pure sample. Moreover, EDX investigations illustrate that the elements used for the preparation of samples distribute homogeneously and the Pr atoms enter into the crystal structure.
- XRD results indicate that there is no remarkable evidence for the forming of second phase. According to this result, the Pr atoms are successfully introduced to the microstructure of the Bi-2212 phase. Furthermore, the lattice parameter a increases while c parameter reduces with the increase in the Pr doping.
- The Load independent microhardness (H_0), elastic modulus (E_0), yield strength (Y_0) and fracture toughness (K_{IC}) are found to be lower than the load dependent values (H_v, E, Y and K_{IC}). Moreover, the Vickers microhardness, elastic modulus, yield strength and fracture toughness values decrease with the increase in the applied load.
- The Vickers hardness of the samples studied exhibits the typical indentation size effect (ISE) behavior.

References

1. P.M. Sarun, S. Vinu, R. Shabna, A. Biju, U. Syamaprasad, Mater. Res. Bull. **44**, 1017 (2009)
2. C. Terzioglu, M. Yilmazlar, O. Ozturk, E. Yanmaz, Physica C **423**, 119 (2005)
3. O. Ozturk, M. Akdogan, H. Aydın, M. Yilmazlar, C. Terzioglu, I. Belenli, Physica B **399**, 94 (2007)
4. C. Terzioglu, O. Ozturk, A. Kilic, A. Gencer, I. Belenli, Physica C **434**, 153 (2006)
5. S.E. Mousavi Ghahfarokhi, M. Zargar Shoushtari, Physica B **405**, 4643 (2010)
6. H. Maeda, Y. Tanaka, M. Fukutomi, T. Asano, Japan. J. Appl. Phys. **27**, L209 (1988)
7. D. Yegen, A. Varilci, M. Yılmazlar, C. Terzioglu, I. Belenli, Physica C **466**, 5 (2007)
8. I. Karaca, S. Celebi, A. Varilci, A.I. Malik, Supercond. Sci. Tech. **16**, 100 (2003)
9. A. Varilci, M. Altunbas, O. Gorur, I. Karaca, S. Celebi, Phys. Status Solidi A **194**, 206 (2002)
10. V. Mihalache, G. Aldica, J. Optoelectron. Adv. M. **9**, 919 (2007)
11. M. Okada, Supercond. Sci. Tech. **13**, 29 (2000)
12. B. Chanda, T.K. Dey, Magn. Supercond. Mater. **A-B**, 295 (2000)
13. M. Runde, IEEE T. Appl. Supercond. **5**, 813 (1995)
14. A. Sedky, Physica C **468**, 1041 (2008)
15. A. Godeke, D. Cheng, D.R. Dietderich, C.D. English, H. Felice, C.R. Hannaford, S.O. Prestemon, G. Sabbi, R.M. Scanlan, Y. Hikichi, J. Nishioka, T. Hasegawa, IEEE T. Appl. Supercond. **18**, 516 (2008)
16. H. Miao, M. Meinesz, B. Czabai, J. Parrell, S. Hong, AIP Conf. Proc. **986**, 423 (2008)
17. A. Biju, R.P. Aloysius, U. Syamaprasad, Supercond. Sci. Tech. **18**, 1454 (2005)
18. K. Koyama, S. Kanno, S. Noguchi, Jpn. J. Appl. Phys. **29**, L53 (1990)

19. S. Vinu, P.M. Sarun, R. Shabna, A. Biju, U. Syamaprasad, J. Appl. Phys. **104**, 043905 (2008)
20. M. Yilmazlar, O. Ozturk, O. Gorur, I. Belenli, C. Terzioglu, Supercond. Sci. Tech. **20**, 365 (2007)
21. S. Vinu, P.M. Sarun, A. Biju, R. Shabna, P. Guruswamy, U. Syamaprasad, Supercond. Sci. Tech. **21**, 045001 (2008)
22. S. Vinu, P.M. Sarun, R. Shabna, A. Biju, U. Syamaprasad, Mater. Lett. **62**, 4421 (2008)
23. R. Shabna, P.M. Sarun, S. Vinu, A. Biju, U. Syamaprasad, Supercond. Sci. Tech. **22**, 045016 (2009)
24. P.M. Sarun, S. Vinu, R. Shabna, A. Biju, U. Syamaprasad, Mater. Lett. **62**, 2725 (2008)
25. R. Shabna, P.M. Sarun, S. Vinu, A. Biju, U. Syamaprasad, J. Alloy. Compd. **493**, 11 (2010)
26. A. Biju, P.M. Sarun, R.P. Aloysius, U. Syamaprasad, J. Alloy. Compd. **454**, 46 (2008)
27. H. Wang, A. Serquis, B. Maiorov, L. Civale, Q.X. Jia, P.N. Arendt, S.R. Foltyn, J.L. Macmanus-driscoll, X. Zhang, J. Appl. Phys. **100**, 053904 (2006)
28. P.M. Sarun, S. Vinu, R. Shabna, A. Biju, U. Syamaprasad, J. Alloy. Compd. **472**, 13 (2009)
29. T. Kucukomeroglu, E. Bacaksiz, C. Terzioglu, A. Varilci, Thin Solid Films **516**, 2913 (2008)
30. J.S. Moodera, R. Meservey, J.E. Tkaczyk, C.X. Hao, G.A. Gibson, P.M. Tedrow, Phys. Rev. B **37**, 619 (1988)
31. A. Biju, U. Syamaprasad, Rao Ashok, J.G. Xu, K.M. Sivakumar, Y.K. Kuo, Physica C **466**, 69 (2007)
32. H.C. Ling, M.F. Yan, J. Appl. Phys. **64**, 1307 (1988)
33. Z. Li, A. Ghosh, A.S. Kobayashi, J. Am. Ceram. Soc. **72**, 904 (1989)
34. A. Leenders, M. Mich, H.C. Freyhard, Physica C **279**, 173 (1997)
35. M. Yilmazlar, H.A. Cetinkara, M. Nursoy, O. Ozturk, C. Terzioglu, Physica C **442**, 101 (2006)
36. K. Hirao, M. Tomozawa, J. Am. Ceram. Soc. **70**, 497 (1987)
37. F. Frohlinch, P. Grau, W. Grellmann, Phys. Status Solidi A **42**, 79 (1977)
38. E.O. Bernhardt, Z. Metall. **33**, 135 (1941)
39. S.M. Khalil, Smart Mater. Struct. **14**, 804 (2005)
40. O. Ozturk, C. Terzioglu, I. Belenli, J. Supercond. Nov. Magn. **24**, 381 (2010)
41. C. Veerender, V.R. Dumke, M. Nagabhooshanam, Phys. Status Solidi A **144**, 299 (1994)
42. R. Rodrıguez, I. Gutıerrez, Mat. Sci. Eng. A Struct. **361**, 377 (2003)
43. U. Kolemen, N. Guclu, O. Uzun, S. Celebi, Physica C **433**, 115 (2005)
44. O. Uzun, U. Kolemen, S. Celebi, N. Guclu, J. Eur. Ceram. Soc. **25**, 969 (2005)
45. O. Ozturk, E. Asikuzun, M. Erdem, G. Yildirim, O. Yildiz, C. Terzioglu, J. Mater. Sci. Mater. El. (2011). doi:10.1007/s10854-011-0429-3
46. O. Ozturk, H.A. Cetinkara, E. Asikuzun, M. Akdogan, M. Yilmazlar, C. Terzioglu, J. Mater. Sci. Mater. El. (2011). doi: 10.1007/s10854-011-0337-6
47. S.M. Khalil, J. Phys. Chem. Solids **62**, 457 (2001)